Int. J. Electrochem. Sci., 7 **(2012)** 1864 - 1883

International Journal of
ELECTROCHEMICAL
SCIENCE
www.electrochemsci.org

Effect of Hydrostatic Pressure on the Corrosion Behavior of Pure Nickel

Bin Liu[1], *Tao Zhang* [1,2,*], *Yawei Shao*[1,2], *Guozhe Meng*[1,2], *Junting Liu*[1], *Fuhui Wang*[1,2]

[1] Corrosion and protection Laboratory, Key Laboratory of Superlight Materials and Surface Technology (Harbin Engineering University), Ministry of Education, Nantong ST 145, Harbin, 150001, China
[2] State Key Laboratory for Corrosion and Protection, Institute of Metal Research, Chinese Academy of Sciences, Wencui RD 62, Shenyang, 110016, China)
[*]E-mail: zhangtao@hrbeu.edu.cn

Received: 29 December 2011 / *Accepted:* 18 February 2012 / *Published:* 1 March 2012

The effect of hydrostatic pressure on the corrosion behavior of nickel in NaCl solution was investigated by electrochemical measurements and OM/SEM observation. The increasing hydrostatic pressure deteriorated the pitting corrosion resistance of nickel, distinguished by the decrease of critical pitting potential (E_{cirt}) with increasing passive current density. The results also demonstrated that hydrostatic pressure had three effects on the corrosion behavior of nickel: (1) the increasing hydrostatic pressure hindered the passive film formation; (2) the increasing hydrostatic pressure retarded the B1 process (parallel birth and death stochastic model) and accelerated the A3 process (parallel birth stochastic model); (3) the pitting growth probability increased

Keywords: Nickel; pitting corrosion; stochastic analysis; infinite element analysis; deep ocean

1. INTRODUCTION

Oil and gas exploitation in deep ocean environment imply challenging harsh corrosive environments for structural materials because of the hydrostatic pressure and the different dissolved oxygen (DO). Thus, the corrosion problem of materials in deep ocean condition must be considered.

Some natural ocean tests reported by American [1-3], Indian [4, 5] and Russian [6, 7] revealed that materials undergo serious corrosion in deep ocean. However, deep ocean environment is a complex system: hydrostatic pressure, different DO, delicately balanced solution of many salts, suspended silt, and decaying organic material. The individual effect of each of the above factors affecting corrosion behavior is not readily distinguishable.

Some researchers devoted to laboratory experiments [9-14] and revealed that an increase in hydrostatic pressure increases the pitting susceptibility of metals, as a result of the conversion of oxides and or hydroxides to soluble hydroxy-chlorides, increased activity of chloride ions and their penetration into the passive film [8-12]. However, some effects of hydrostatic pressure on the corrosion behavior of materials are not well known, including its effect on the pitting corrosion resistance, such as pitting potential and passive current density, on the nature of passive film, such as electronic structure, density of point defect and diffusivity of point defect, on the pitting initiation process and on the pitting generation mechanism.

Pitting corrosion is a complicated phenomenon. The pitting generation event has been widely known to be a stochastic nature [15]. Recently, stochastic analysis has been proposed to investigate the pitting initiation processes. Localized corrosion of different metals or alloys in various systems has been characterized in terms of stochastic analysis [16-27].

In the present work, the corrosion behavior of pure nickel was investigated in 3.5% NaCl solution at different hydrostatic pressures with other parameters unchanged (DO, temperature, etc.). The effect of hydrostatic pressure on the corrosion of nickel was discussed.

2. EXPERIMENTAL METHOD

2.1. Materials

The specimen for this study was commercial pure nickel, the composition of which was, <0.05% Co, <0.001% Cu, <0.003% C, <0.003% S, <0.003% P, Ni balance. The specimens with dimension 10×10×10mm, the sealing method is described as following: first, the specimens are mounted in the vacuum chamber about 1-2 min at 40 °C (the pressure is lower than 1 atm), so that the bubble could desorb from the specimen surface. Second, specimens are cured at 60 °C for 12 h. This cured epoxy had a higher adhesive ability on the nickel sample. All of the specimens were wet ground to a 1000-grit finish, degreased with acetone, cleansed with distilled water and dried in a compressed hot air flow. The test solution was 3.5% NaCl and prepared by analysis grade chemicals and distilled water. The test solution was saturated in air at one atmosphere and the content of DO was determined by oxygen analyzer. DO content was controlled by the deaeration with nitrogen until the oxygen content achieved to 6.5 ppm. The temperature of test solution is about 25 ℃ and controlled by jacketed cooler.

2.2. Experimental setup

The pressure vessel was shown in Fig. 1, which was pressurized with a hydropneumatic pump by using high purity nitrogen. According to Henry' law, it can be believed that the oxygen pressure was unchanged with the increasing of nitrogen pressure. Nitrogen pressure had no influence on the DO concentration.

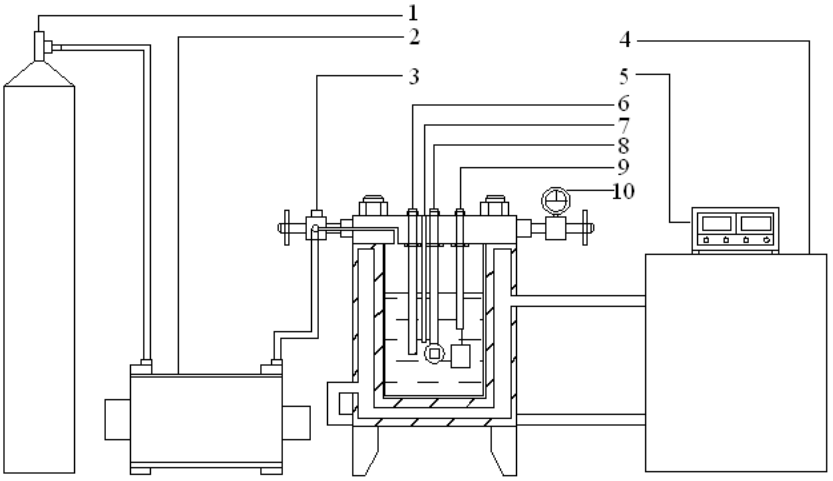

Figure 1. Schematic diagram of the experimental setup for deep ocean corrosion study. (1) nitrogen vessel, (2) hydropneumatic pump, (3) valve, (4) cooling equipment, (5) temperature monitor, (6) solid-reference-electrode, (7) thermocouple, (8) working electrode, (9) counter electrode and (10) pressure meter.

2.3. Electrochemical measurements

For all the experiments, a three-electrode cell was used with a counter electrode of platinum (20mm×20mm) and an Ag/AgCl reference electrode. The potential of the Ag/AgCl reference electrode was compared (within the pressure range 1-100 atm) with that of identical electrode maintained at 1 atm. The slight change (-5mV at 100 atm) of the pressurized Ag/AgCl reference electrode potential was noted in further measurements of the working electrode potential at various pressures. The test pressures were 1 atm and 80 atm.

The potentiodynamic polarization technique was used to determine the pitting potential of nickel. Different potential sweep velocities of 1mV/s, 3mV/s, 5mV/s were applied in the potentiodynamic polarization tests, which were carried out using a model 273A potentiostat (EG&G). At least thirty replicates were used for each potential sweep velocity. Prior to all electrochemical measurements, the specimens were initially reduced potentiostatically at $-1V_{Ag/AgCl}$ for 1 min to remove air-formed oxides from the surface [28] and then kept for 1 h in the NaCl solution at various hydrostatic pressures.

Induction time of nickel at various hydrostatic pressures was determined by chronoamperometry curve under a constant potential of 200 $mV_{Ag/AgCl}$. Thirty replicates were used for the specimens.

2.4. Microstructure observation

2.4.1. SEM

The pitting morphology of nickel after the potentiostatic measurements were studied by means of X-Max SEM.

2.4.2. Pitting mouth size and pitting depth measurement

The specimen tested was gently rinsed and dried for examination with an optical microscope. Before the optical observation, the specimen was treated by ultrasonic treatment, in order to remove the lacy covered on the pitting mouth. The size of the pitting mouth *s* was determined from photography by measuring the area of the pitting mouth with a planimeter in the microscope. The estimated error in *s* is 5%. Pitting depths *h*, which were treated with ultrasound to rupture the pitting lacy, were measured by applying the Fine Focus Technique [29], where the distances required shifting the optical objective between the focal points on the original surface of a sample and on the bottom of the pitting were compared. The estimated error in *h* is 1μm.

2.5. Finite element models

The localized stress distributions around pitting were calculated using commercial ANSYS finite element software. 3D solid model of single artificial hemispherical pitting was modeled in the ANSYS pre-processor. Typical 3D sizes of pit (based on statistical results) were used in the finite element models. Radius of 3D solid model is 150μm. An elastic material model was used in the finite element models. Elastic material model included the Young's modulus (206 GPa) and a Poisson's ratio (0.31). Hexahedral elements with 20-node quadratic brick, reduced integration were used to represent the model for stress analysis. Boundary conditions were applied to the top surface of the specimen to ensure specimen alignment during pressurization. The boundary conditions are such that the only direction in which the top surfaces of the specimen can move is the axial one.

3. RESULTS AND DISCUSSION

3.1. Effect of hydrostatic pressure on the corrosion resistance of Ni

3.1.1. Effect of hydrostatic pressure on the pitting potential of Ni

The polarization curves of nickel at each of the two hydrostatic test pressures were exhibited in Fig. 2. On the presented curves for each electrode, a pitting potential could be determined. It could be found that the pitting potential data were scatted. The distributions of pitting potential for nickel at each of the two hydrostatic test pressures were plotted as illustrated in Fig. 3. Cumulative probability shown in a vertical abscissa was calculated by a mean rank method:

$$P_{cum} = i/(N+1) \qquad (1)$$

Where P_{cum} is the cumulative probability of measured pitting potential (E_{pit}), i is the order in the total number N (i = 1, 2, 3, …, N). All of the pitting potential distributions exhibited a linear

behavior, indicating that the distribution of pitting potentials measured followed the normal probability distribution.

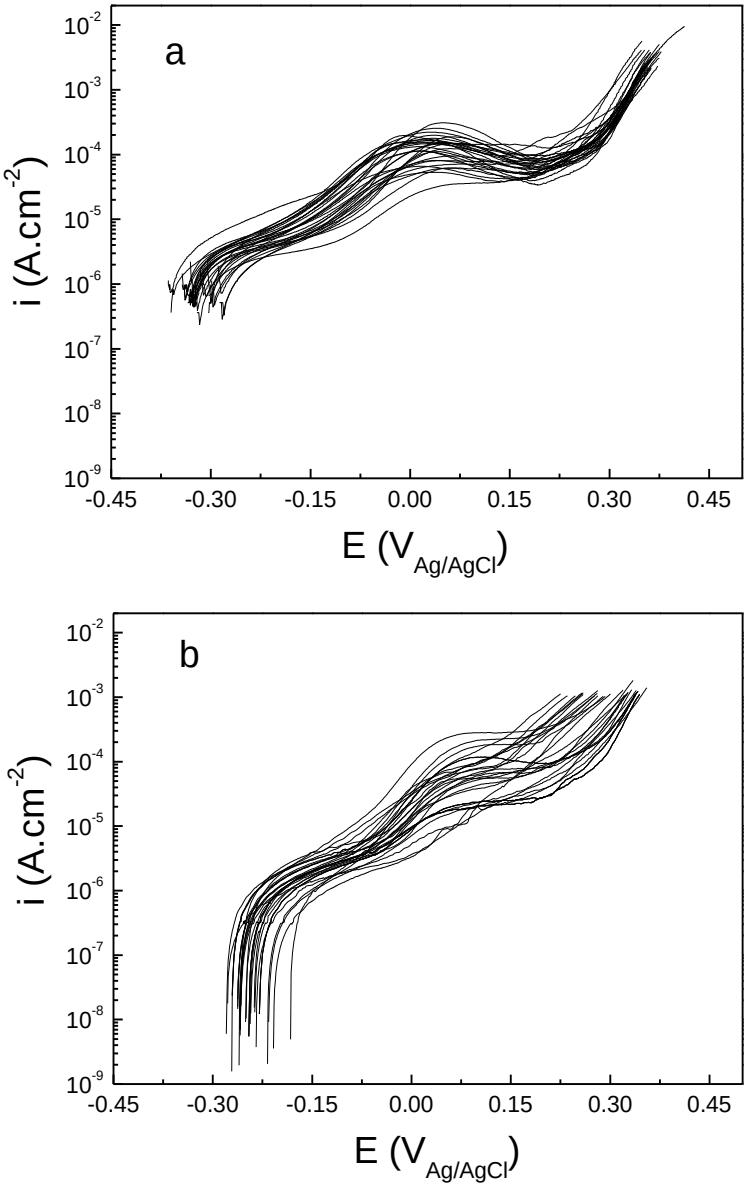

Figure 2. Potentiodynamic polarization curves of nickel at (a)1 atm and (b) 80 atm hydrostatic pressures with scanning rate of 1 mV/s.

The median of distribution E_m, decided at P = 50%, was determined from Fig. 3. As can be seen from Fig. 3, the pitting potential E_m, shifts to the negative direction with hydrostatic pressure (decreased from 188 mV to 176 mV), suggesting that the increase of hydrostatic pressure increased the pitting susceptibility of nickel.

The distribution of average passive current density, $i_{passive}$, measured at different hydrostatic pressures was demonstrated in Fig. 4. It was found that the distribution of $i_{passive}$ shifted to a higher current region with the increasing of hydrostatic pressure.

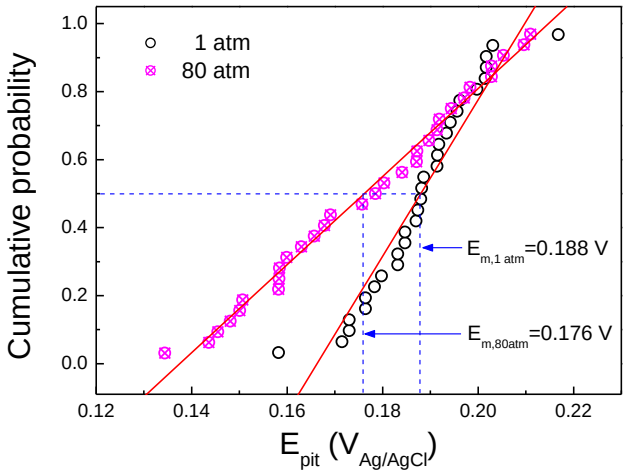

Figure 3. The distribution of pitting potential of nickel at (a) 1atm and (b) 80 atm hydrostatic pressure.

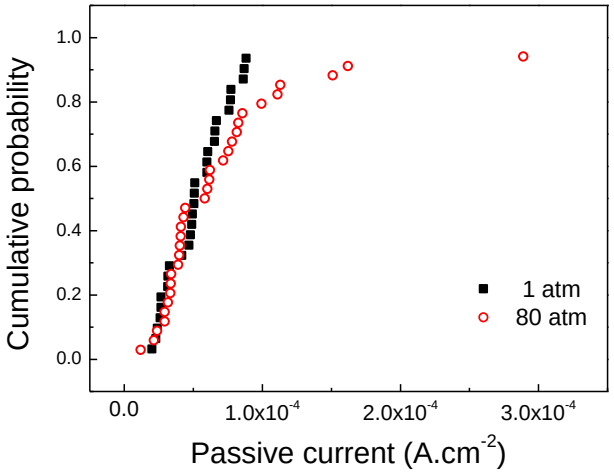

Figure 4. The distribution of average passive current density at various hydrostatic pressures.

The decrease of E_m with increasing passive current density indicated that the corrosion resistance was deteriorated with the increase of hydrostatic pressure. It is well known there are certain relationships between the corrosion resistance of metal and the properties of passive film [28]. Therefore, this implied that the properties of passive film on nickel changed obviously with the increase of hydrostatic pressure.

3.2. Effect of hydrostatic pressure on the formation of passive film of Ni

Typical chronoamperometry curves for nickel at various hydrostatic pressures at a potential of 200 $mV_{Ag/AgCl}$ were shown in Fig. 5. It can be seen that, each of the "current-time" curves consists of an initial spike (within the first 0.8 s) due to the charging of the electrochemical double layer [30, 31], a subsequently rising portion due to the nucleation process and a posterior decreasing portion due to

the diffusion process. During this stage of the formation of the passive film, the nuclei develop diffusion zones around themselves and as these zones overlap the transient current decreases rapidly due to the poor electroconductance of the passive film and reach steady state current.

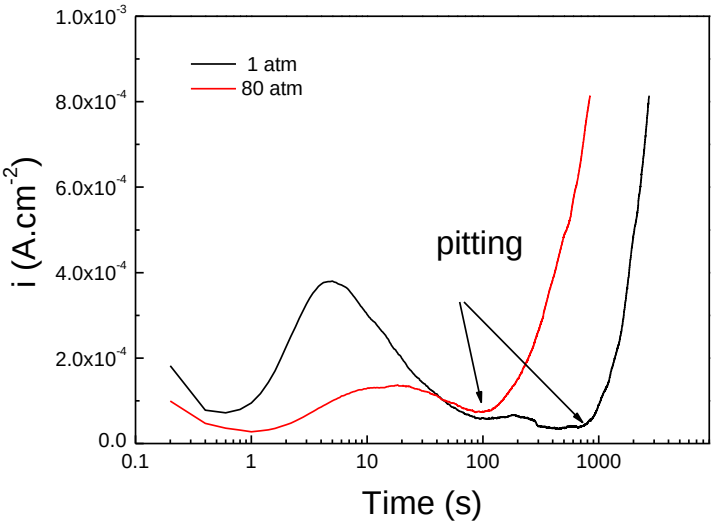

Figure 5. Typical chronoamperometry curves for nickel at various hydrostatic pressures at a potential of 200mV

Considering the current transients observed in the course of the formation of passive films, a suitable model for the formation mechanism of passive film seems to be the overlapping of two growth steps.

One step is instantaneous nucleation process, 2D growth, determined by the lattice incorporation onto the periphery of a growing nucleus and taking into account the overlap of nuclei [32]. The current-time transient for this instantaneous nucleation process had been shown [32, 33] as follows:

$$i_{2D} = \frac{2\pi nFMhN_0k_g^2t}{\rho}\exp[-\frac{\pi N_0M^2k_g^2t^2}{\rho^2}] \qquad (2)$$

This equation predicts a maximum in the current-time curve with

$$t_m = (\frac{\rho^2}{2\pi N_0M^2k_g^2})^{1/2} \qquad (3)$$

and

$$i_m = nFhk_g(2\pi N_0)^{1/2}\exp(-\frac{1}{2}) \qquad (4)$$

The other step is progressive nucleation process, 3D growth, the nucleation of pyramids at a constant rate on the substrate which grow in three dimensions. The current–time transient for the case where the pyramids are of right circular cone type has been shown to be [34]:

$$i_{3D} = nFk_2[1-\exp(\frac{-\pi M^2 k_1^2 At^3}{3\rho^2})]\exp(\frac{-\pi M^2 k_1^2 At^3}{3\rho^2}) \qquad (5)$$

This predicts a maximum in the current–time curve with

$$t_m = (\frac{3\rho^2 \ln 2}{\pi M^2 k_1^2 A})^{1/3} \qquad (6)$$

and

$$i_m = \frac{nFk_2}{4} \qquad (7)$$

In the above equations, N_0 is the number density of active sites, k_g is the lateral growth rate constant of nuclei, A is the nucleation rate constant, M is the molecular weight (74.70 g/mol), ρ is the density of the deposited material (NiO 6.827 g/cm^3, Ni(OH)$_2$ 4.150 g/cm^3), h is the thickness of the deposited layer, k_1 and k_2 are the rate constants for parallel and perpendicular growth with respect to the electrode surface and nF refers to the molar charge transferred during the process.

In Fig.6, the non-dimensional i/i_m was plotted as a function of t/t_m, for the passive film formation of nickel at various hydrostatic pressures. The experimental i/i_m–t/t_m curves seem to follow the theoretical instantaneous nucleation curve more closely at each of the two hydrostatic test pressures, which indicated instantaneous nucleation was more possible to proceed under that condition. In the other word, hydrostatic pressure had no influence on the formation mechanism of passive film on nickel surface.

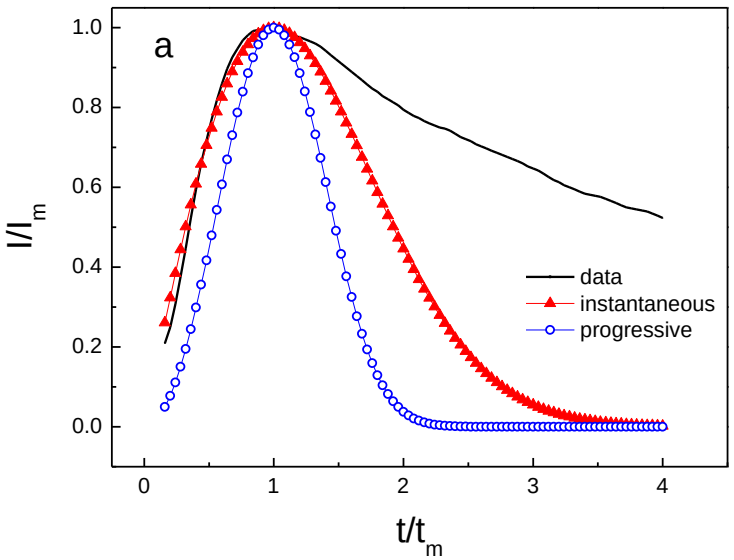

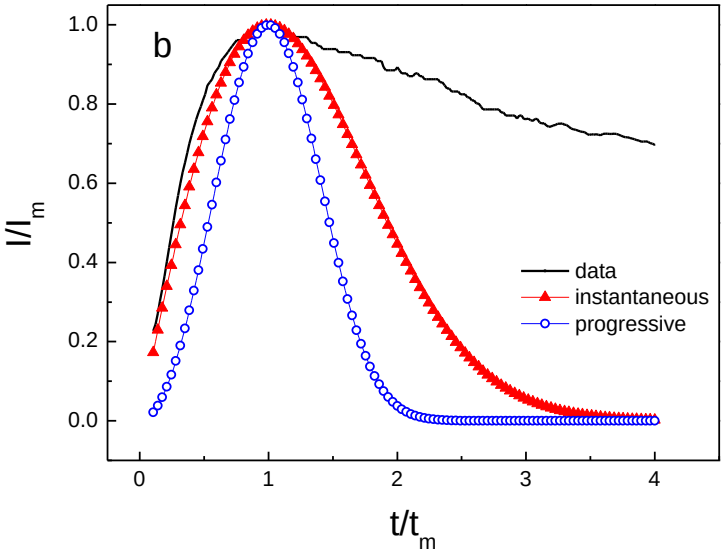

Figure 6. The non-dimensional i/i_m is plotted as a function of t/t_m, for the passive film formation of nickel at (a) 1atm and (b) 80 atm hydrostatic pressures.

However, it was noticed that the t_m of nickel at 80 atm (11.4 s) was longer than that at 1 atm (5 s). The important kinetic parameters, $N_0K_g^2$, were calculated according to instantaneous nucleation theoretical model (Eqn.3). $N_0K_g^2$ implied the formation rate of passive film [31]. With the increase of hydrostatic pressure (from 1 to 80 atm), if assumed the composition of passive film was NiO, the value of $N_0K_g^2$ should decrease from 5.32×10^{-5} to 1.02×10^{-5} $mol^2.cm^{-6}.s^{-2}$; if assumed the composition of passive film was $Ni(OH)_2$, the value of $N_0K_g^2$ should decrease from 1.97×10^{-5} to 3.78×10^{-6} $mol^2.cm^{-6}.s^{-2}$. A. Beccaria [10] revealed that the percent of $Ni(OH)_2$ in passive film increased with the increasing hydrostatic, so, it could be confirmed that the the value of $N_0K_g^2$ decreased with hydrostatic pressure, which implied that the increasing hydrostatic pressure hindered the formation of passive film.

3.3. Effect of hydrostatic pressure on the pitting formation of Ni

3.3.1. The stochastic model for pitting formation

The time when current increases rapidly is the induction time (τ). Repetition of the same experiment yielded a number of induction time values.

The pitting formation event has been widely known to be a stochastic process. T. Shibata presented a stochastic theory of pitting corrosion based upon sensitivity analysis of parameters in the stochastic model that could rationally explain stochastic distributions of induction time for pitting formation [16-23]. In the stochastic model, the pitting formation process does not fit a simple exponential distribution, but could be explained by assuming series or parallel combinations of the simple birth stochastic process and birth/death process. The proposed models can be divided into two groups [16-23]:

Type A: Pure birth stochastic models, which only consider pitting generation events;

Type B: Birth and death stochastic models, which assume stochastic pitting generation and pitting repassivation.

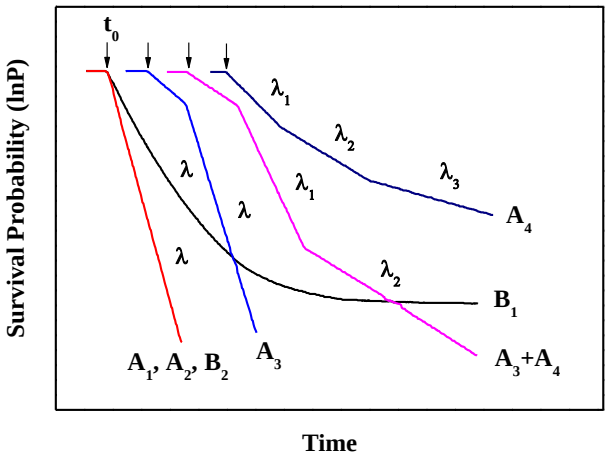

Figure 7. A schematic illustration of ln P_{sur} vs time of various stochastic models.

The expected equations for the survival probability, $P_{sur,}$ and time for pitting formation formulated for each model are shown in Table1 [16-23] and corresponding curves between ln(P_{sur}) and time for each mode are illustrated in Fig. 7 [16-23].

Table 1. Analytical expressions of the survival probability function for various stochastic models.

Model	Survival probability function
Birth process	
A1 simple	$P(t)=\exp[-\lambda(t-t_0)]$ [16-23]
A2 series	$P(t)=\exp[-m\lambda(t-t_0)]$ [16-23]
A3 parallel	$P(t) =1-\{1-\exp[-\lambda(t-t_0)]\}^m$ [16-23]
A4 combination	$P(t) = \Sigma f_i \exp[-\lambda_i(t-t_0)]$ [16-23]
Birth and death process	
B1 parallel	$P(t) =\mu/(\lambda+\mu) +\lambda/(\lambda+\mu) \exp[-(\lambda+\mu) (t-t_0)]$ [16-23]
B2 series	$P(t) = \exp[-\alpha\lambda(t-\tau_c) \exp (-\mu\tau_c)]$ [16-23]

3.3.2. Effect of hydrostatic pressure on the mechanism of pitting formation

Fig. 8 showed the logarithm of the survival probability, P_{sur}, as a function of induction time, t, for nickel at 1 atm and 80 atm, respectively.

This distribution type was the specific character of the combination of B1 model (parallel birth and death stochastic model) and A3 model (parallel birth stochastic model), which was expressed as the following equation:

$$P(t)=\frac{\mu_{B1}}{(\mu_{B1}+\lambda_{B1})}+\frac{\lambda_{B1}}{(\mu_{B1}+\lambda_{B1})}\exp[-(\lambda_{B1}+\mu_{B1})(t-t_0)]+1-\{1-\exp[-\lambda_{A3}(t-t_0)]\}^m \quad (9)$$

where λ_{B1} and μ_{B1} are the pitting generation rate and pitting repassivation rate of B1 model, respectively, λ_{A3} is the pitting generation rate of A3 model, and t_0 is the incubation time, before which no pitting generation probability was expected. The parameters (λ_{B1}, μ_{B1} and λ_{A3}) were calculated and shown in Table 2.

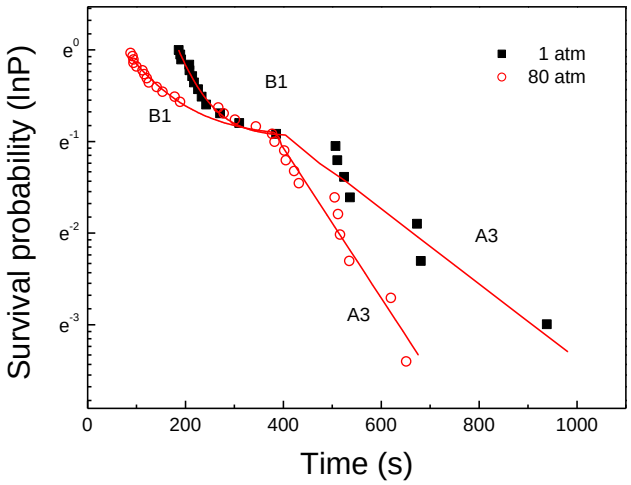

Figure 8. Plots of survival probability, P_{sur}, vs time for nickel at various hydrostatic pressures.

Table 2. The parameters for the stochastic model.

Hydrostatic pressure (atm)	Stochastic model	λ_{A3} (s^{-1})	λ_{B1} (s^{-1})	μ_{B1} (s^{-1})
1	A3+B1	2.95×10^{-3}	5.15×10^{-1}	7.76×10^{-3}
80	A3+B1	8.18×10^{-3}	8.52×10^{-3}	2.34×10^{-3}

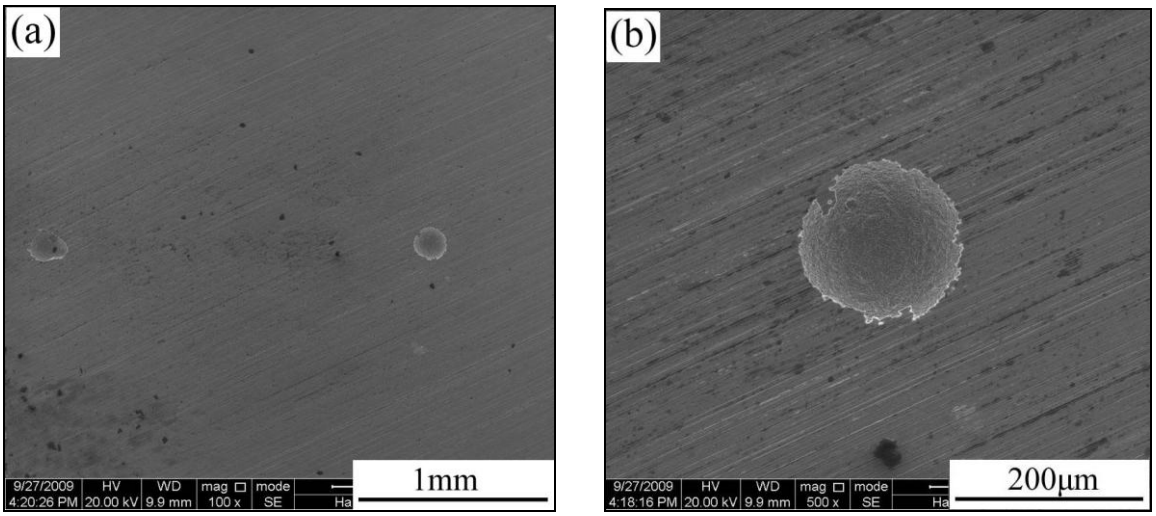

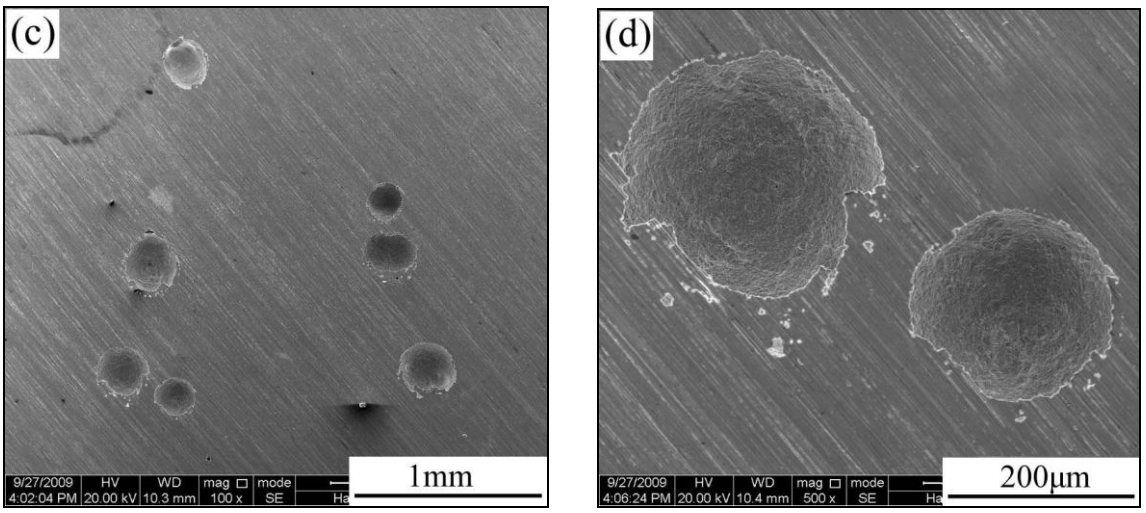

Figure 9. The pitting corrosion morphology of nickel (a) small magnification and (b) large magnification at 1 atm, (c) small magnification and (d) large magnification at 80 atm hydrostatic pressures.

According to Fig.9 and Table 2, two kinds of information could be obtained. Firstly, plots of the distribution of induction time for nickel at each of the two hydrostatic test pressures exhibited analogue shape, which suggested that hydrostatic pressure did not change the mechanism of pitting formation. Secondly, hydrostatic pressure had different influence on the pitting generation process of B1 and A3 model, respectively. For B1 process, the increasing of hydrostatic pressure retarded the B1 process, the pitting generation rate, λ_{B1}, and pitting repassivation rate, μ_{B1}, decreased from 5.15×10^{-1} and 7.76×10^{-3} s^{-1} (1 atm) to 8.52×10^{-3} and 2.34×10^{-3} s^{-1} (80 atm), respectively. For A3 process, the increasing of hydrostatic pressure accelerated it. With the increasing of the hydrostatic pressure, the pitting generation rate, λ_{A3}, increased from 2.95×10^{-3} to 8.18×10^{-3} s^{-1}.

3.4. Effect of hydrostatic pressure on the pitting morphology and geometry

With the increasing hydrostatic pressure, the pitting cavity spreads over nickel surface, Fig.9. For example, in the condition of atmospheric pressure, the average pitting number is about 3.16/cm^2; while in case of 80 atm hydrostatic pressure, the average pitting number increases to 12.57/cm^2. Whether at atmospheric pressure or not, the notable feature of pitting cavity is etching interior surface indicating the absence of salt-film precipitation [35].

Some scientists suggested that the pitting geometry could be described by the ratio of pitting mouth size *s* and pitting depth *h* (*s*/2*h*) [36-38]:

$s/2h < 1$, pitting geometry exhibits bullet shape;

$s/2h = 1$, pitting geometry shows hemispherical shape;

$s/2h > 1$, pitting geometry demonstrates shallow-disk shape;

The schematic illustration of pitting geometry was exhibited in Fig.10.

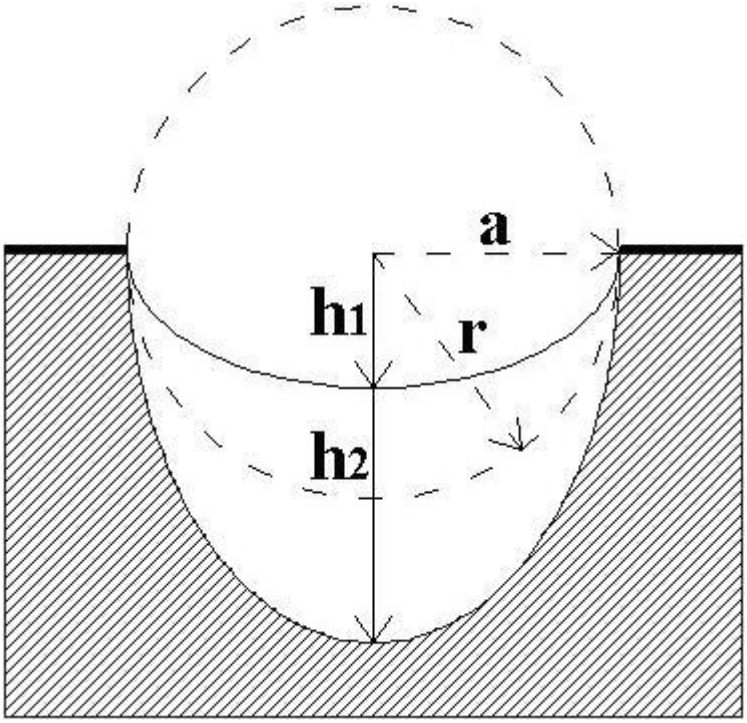

Figure 10. A schematic illustration of pitting geometry, *s*/2*h* <1, pitting geometry exhibits bullet shape; *s*/2*h* =1, pitting geometry shows hemispherical shape; *s*/2*h* >1, pitting geometry demonstrates shallow-disk shape.

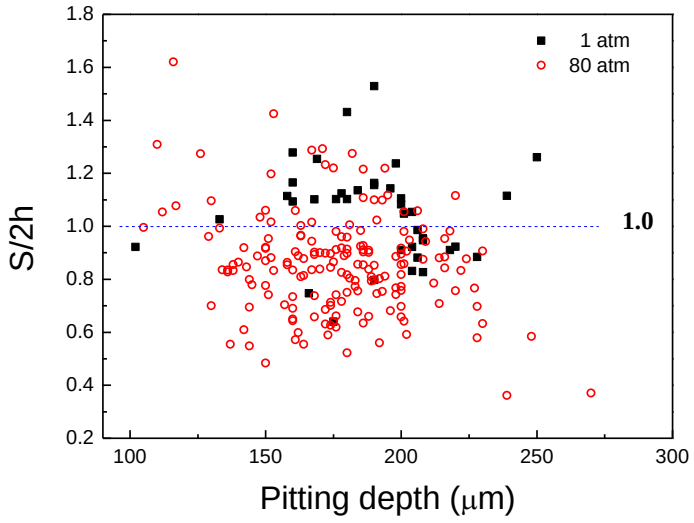

Figure 11. The pitting geometry of nickel at different hydrostatic pressure.

Fig.11 showed the pitting geometry of nickel at each of the two hydrostatic test pressures. The ratio of measured pit mouth width to depth *s*/2*h* did depend upon the hydrostatic pressure and decreased markedly with increasing hydrostatic pressure. Fig.12 showed the statistic result of Fig.11.

At 1 atm, the value of *s*/2*h* accumulated around 0.95 and 1.2, respectively, which indicated that the pitting geometry of pure nickel was distinguished by hemispherical shape and shallow-disk shape.

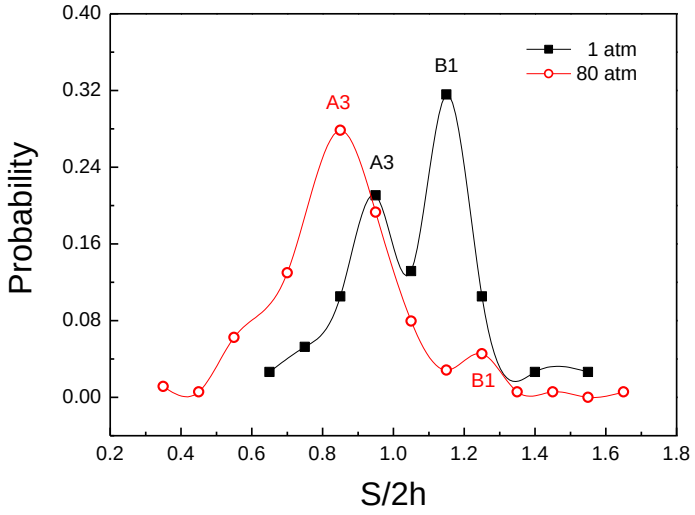

Figure 12. Distribution of pitting geometry predicted by statistical analysis from Fig.11.

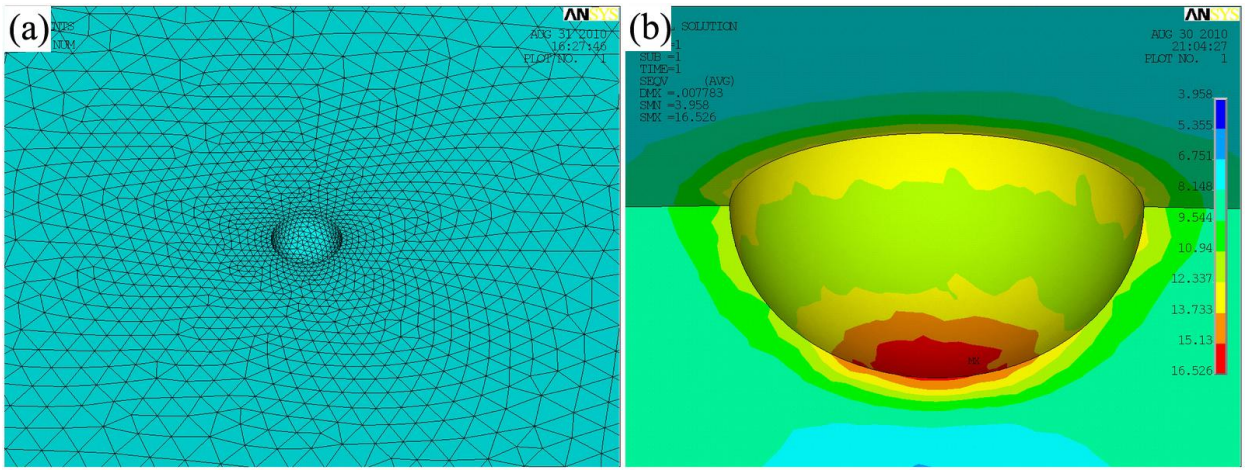

Figure 13. Specimen geometry with mesh structure around 300 μm pit highlighted (a), and 3D localized stress intensity distributions in and around hemispherical pitting cavity (b).

However, with the increasing hydrostatic pressure, most of *s*/2*h* data distributed around 0.85, meanwhile, a little of *s*/2*h* data distributed around 1.25, implying the most of pitting cavity characterized as bullet shape in case of higher hydrostatic pressure. In brief, the statistic result indicated that the hydrostatic pressure had significant influence on the type of pitting geometry. The increasing hydrostatic pressure increased the probability of bullet shape pitting cavity, while decreased the probability of shallow-disk shape pitting cavity.

In order to better understanding the effect of hydrostatic pressure on the pitting geometry, localized stress distributions of pitting was simulated by finite element method. A hydrostatic pressure

of 80 atm was applied to the top surface of the model. Loading direction is vertical to pitting (Fig. 13a). The 3D stress intensity distribution of pitting was shown in Fig. 13b. It was clearly seen that the stress concentration zones of pitting bottom was much larger than that of pitting mouth. X. Liu et al. [39] revealed that the stress led to the acceleration of anodic dissolution rate. Therefore, Fig.13b implied that the hydrostatic pressure evoked the anisotropic 3D growth of pitting, and the corrosion rate of cavity bottom was higher than that of cavity mouth. This should be the reason why the pitting geometry changed from hemispherical shape to bullet shape with the increase of hydrostatic pressure.

Moreover, stochastic analysis results (Fig.8) indicated that the increasing hydrostatic pressure retarded the pitting generation process of B1 model and accelerated the A3 model. Combining the results of pitting generation mechanism and pitting geometry, it implied that bullet shape pitting cavity might correspond to the pitting generation process of A3 model; shallow-disk shape pitting cavity might be corresponding to the pitting generation process of B1 model.

3.5. Effect of hydrostatic pressure on the pitting growth

After the induction time, a sudden current rise was observed, which suggested that a stable pitting had formed and grown. Pitting growth is usually modeled using a nonhomogeneous Markov process [40]. To do this, the theoretical foundations of extreme value statistics have been employed. It is shown that the solution of the Kolmogorov forward equations, governing the growth of an individual pitting, is in the domain of attraction of the Gumbel distribution [40]. In many applications, the Gumbel Type distribution has been claimed to account for the stochastic nature in the observed behavior of corrosion systems [40-44].

The extreme value statistics analysis can be estimated according to the following procedure [44]: first, all calculated extreme value data are arranged in order from the smallest, and then the probability F(Y) is calculated as 1-[M/(N + 1)], where M is the rank in the ordered extreme value and N the total number of extreme value data. The reduced variant (Y) can be calculated by the formula Y=-ln {-ln [F(Y)]}.

The probability that the largest value of pitting depth is described by a double exponent (Gumbel Type extreme value distribution) can be calculated by the following form equations [44].

$$Pit_{\max} = \mu + \alpha \ln S \qquad (10)$$

$$\text{Probability of pitting depth} = 1 - \exp\{-\exp[\frac{-(\text{pitting depth} - [\mu + \alpha \ln S])}{\alpha}]\} \qquad (11)$$

where μ is the central parameter (the most frequent value), S is the specimen area and α is the scale parameter, which defines the width of the distribution.

The largest pitting depth within each of the potentiostatic measurements were determined by Fine Focus Technique [29] and the values were subjected to extreme value statistics analysis. The values of the reduced variant were plotted against the ordered pitting depth in Fig.14. Fig.14 distinctly

showed two linear regions in one plot, which indicated that two kinds of pitting growth mechanism (bullet shape and shallow-disk shape) undertook on nickel surface.

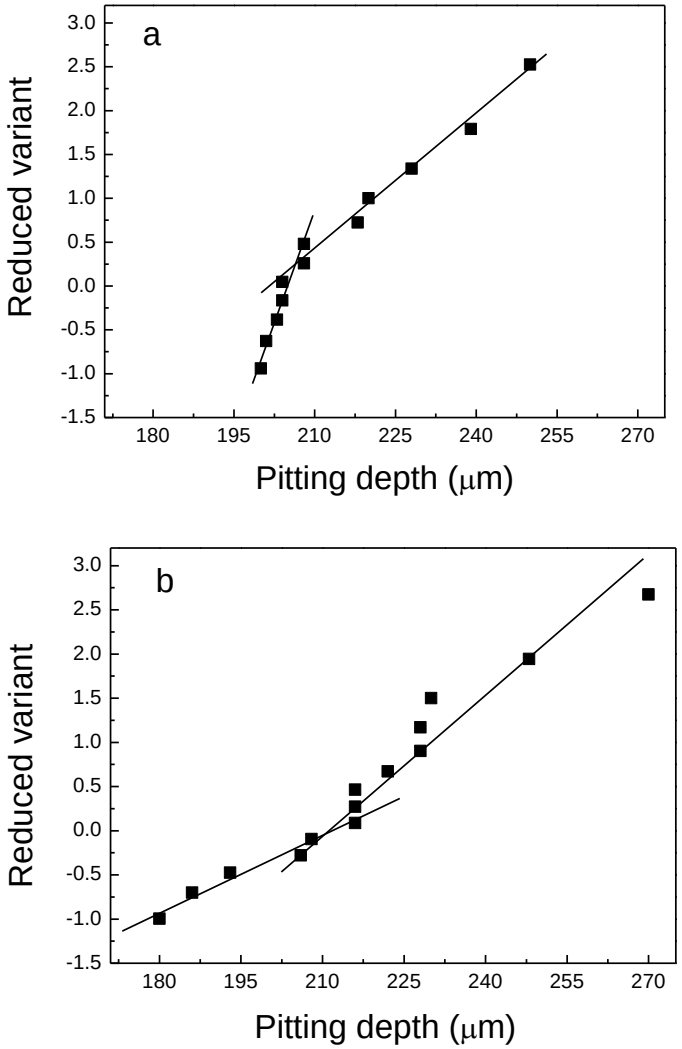

Figure 14. Gumbel probability plots of nickel (a) 1atm and (b) 80 atm hydrostatic pressures.

The observation of straight line confirmed that the experimental data did in fact fit the Gumbel distribution. The values of α and μ are the scale and location parameters for the distribution of the largest pits respectively.

These values are analogous to the standard deviation and average, and describe the shape and centre of the probability distribution of the maximum stable pitting depth expected from electrodes identical to those used for the measurements and are treated in the same manner for the same period of time. The scale and location parameters measured under various hydrostatic pressures were shown in Table 3. The maximum pitting depth distributions of pure nickel at each of the two hydrostatic test pressures were graphically represented in Fig. 15.

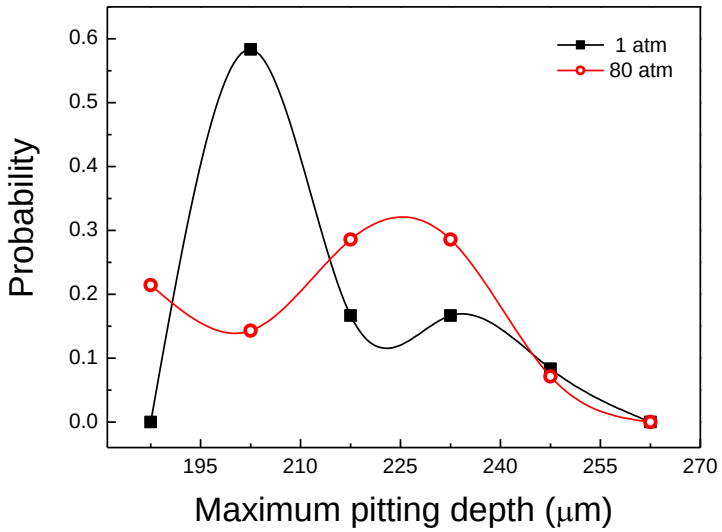

Figure 15. The distributions of maximum pitting depth of nickel at each of the two hydrostatic pressures.

Table 3. Gumbel distribution parameters for nickel at various hydrostatic pressures

Hydrostatic pressure (atm)	Maximum pitting depth (μm)	Location parameters μ	Scale parameters α
1	d >208	201.31	19.93
	d <208	204.42	4.86
80	d >216	211.30	13.30
	d <216	206.62	22.15

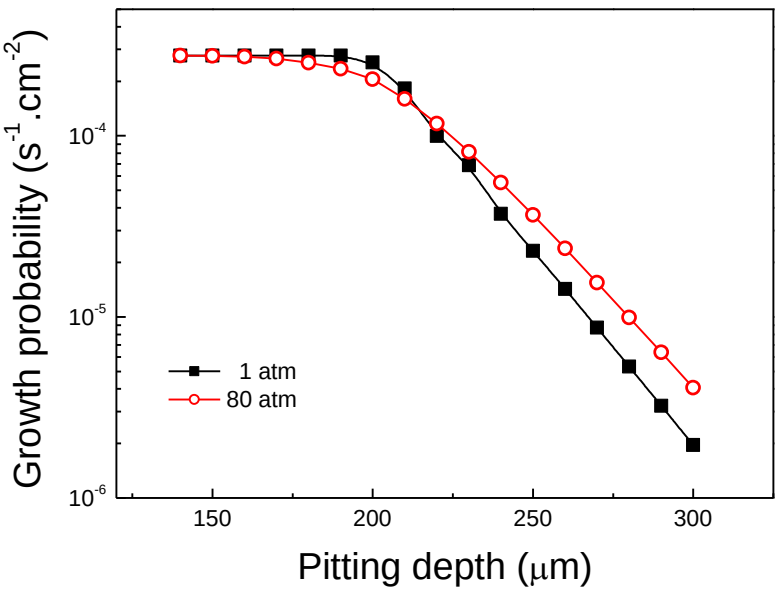

Figure 16. Probabilities of various depth pittings occurring on nickel at various hydrostatic pressures.

The probability of a given pitting depth occurring under each of the two hydrostatic test pressures was calculated using Eq. (11) and the results were shown in Fig. 16. The probabilities could be converted into an expected time for a pitting cavity with a particular depth to occur by taking the reciprocal of the probability. That is, calculating the time it takes for the cumulation of the probabilities to equal unity. For example, a 200 μm pitting depth under 1 atm hydrostatic pressure will occur on average after 65 min, but under 80 atm hydrostatic pressure, the average time for the same 200 μm pitting depth to occur is 81 min. A 300 μm pitting depth under 1 atm hydrostatic pressure will occur on average after 142 h, but under under 80 atm hydrostatic pressure the average time for the same 300 μm pitting depth to occur is 68 h. These results indicate that a pitting formed on nickel had a higher probability of developing into a larger pitting cavity at higher hydrostatic pressure than at lower hydrostatic pressure.

A simple model of the pitting growth kinetics is proposed for better understanding the effect of hydrostatic pressure on the pitting growth process. When the pitting was in the active (salt-free) state, the overpotential of pitting, $\eta_{pitting}$, could be expressed as:

$$\eta_{pitting} = E_{potentiostatic} - E_{corr,pitting} - IR_s \qquad (12)$$

where $E_{potentiostatic}$ is the potentiostatic potential, $E_{corr,\ pitting}$ is the corrosion potential in pitting environment and solution resistance drop is IR_s.

As mentioned in the section 3.4, the stress localized towards pitting bottom with the increase of hydrostatic pressure. The increasing stress concentration increased the anodic dissolution rate [39], which indicated the decrease of the corrosion potential ($E_{corr,\ pitting}$) in pitting environment.

On the other hand, for the potential drop, IR_s, the total solution resistance, R_s, is given by Eq. (13) where R_{int} is the solution resistance within the pitting cavity and R_{ext}, is the resistance of the external solution [45]. The resistivity of pitting solution can be represented by an average resistivity, ρ, and then a pit of radius r and depth L has an internal resistance given by Eq. (14). The external solution resistance can be calculated by Eq. (15) which gives the resistance from specimen to a counter electrode at infinity in a solution of resistivity ρ'.

$$R_s = R_{\text{int}} + R_{ext} \qquad (13)$$

$$R_{\text{int}} = \frac{\rho \cdot L}{\pi \cdot r^2} \qquad (14)$$

$$R_{ext} = \frac{\rho'}{4 \cdot r} \qquad (15)$$

In the condition of the same pitting depth, L, the pitting radius (r) of bullet shape pitting cavity is lower than that of hemispherical pitting cavity. Assuming the ρ and ρ' at two hydrostatic test pressures are same. In case of same current flow, I, the IR_s at 80 atm hydrostatic pressure was higher than that at atmospheric pressure.

The above discussion indicated that the hydrostatic pressure had two competitive influences on the pitting growth process. On one hand, the increasing hydrostatic pressure led to the stress localization towards pitting bottom, which induced the increase of pitting growth rate and bullet shape cavity; on the other hand, the bullet shape cavity increased the potential drop of solution, which deceased the pitting growth rate. However, stress localization effect had greater influence on the pitting growth rate than that of potential drop effect, which led to the increase of pitting growth probability with increasing hydrostatic pressure.

4. CONCLUSION

The corrosion resistance of nickel was deteriorated in the presence of higher hydrostatic pressure, which was characterized by the decrease of E_{cirt} and the increase of passive current density.

The formation of passive film at various hydrostatic pressures followed instantaneous nucleation (2D) mechanism. The increasing hydrostatic pressure had no effect on the passive film formation mechanism, but hindered the formation of passive film.

The pitting generation mechanism was the combination of B1 model (parallel birth and death stochastic model) and A3 model (parallel birth stochastic model). B1 and A3 model related to shallow-disk shape and bullet shape pitting cavity, respectively. The increasing hydrostatic pressure retarded the B1 process, meanwhile, accelerated the pitting generation process of A3 model. At higher hydrostatic pressure, most of pitting geometry became bullet shape.

The increasing hydrostatic pressure increased the pitting growth probability. In case of higher hydrostatic pressure, pitting on nickel surface was easier to develop into a deeper cavity.

ACKNOWLEDGMENT

The authors wish to acknowledge the financial support of the program for New Century Excellent Talents in University of China (NCET-09-0052), the National Natural Science Foundation of China (No. 50771038), the Fundamental Research Funds for the Central Universities (HEUCF102012001), the Excellent Young Scholars of Higher University of Heilongjiang Province (1153G061).

References

1. M. Schumacher: ‘Sea water corrosion handbook’, New Jersey, Noyes Data, 1979, 107-964.
2. S. Dexter, *Corros.* 36 (1980) 423.
3. S. Chen, W. Hartt, S. Wolfson, *Corros*., 59 (2003) 721.
4. R. Venkatesan, M. Venkatasamy, T. Bhaskaran, E. Dwarakadasa, E. Dwarakadasa, Briti. *Corros. J.*, 37 (2002) 257.
5. S. Sawant, A. Wagh, *Corros. Prevent. Contr*. 37 (1990) 154.
6. I. Ulanovskii, *Prot. Met.* 15 (1979) 563.
7. I. Ulanovskii, V. Egorova, *Prot. Met*. 14 (1978) 137.
8. A. Beccaria, G. Poggi, G. Castello, *Briti. Corros. J*., 21 (1986) 19.
9. A. Beccaria, P. Fiordiponti, D. Mattongno, *Corros. Sci*., 29 (1989) 403.
10. A. Beccaria, G. Poggi, M. Arfelli, D. Mattongno, *Corros. Sci*., 34 (1993) 989.

11. A. Beccaria, G. Poggi, D. Gingaud, G. Castello, *Briti. Corros. J*., 29 (1994) 65.
12. A. Beccaria, G. Poggi, G. Castello, *Briti. Corros. J*., 30 (1995) 283.
13. S. Chen, W. Hartt, *Corros.*, 58 (2002) 38.
14. T. Zhang, Y. Yang, Y. Shao, G. Meng, F. Wang, *Electrochim. Acta***,** 54 (2009) 3519.
15. T. Shibata, T. Takeyama, *Nature***,** 260 (1976) 315.
16. T. Shibata, *Corros.*, 52 (1996) 813.
17. T. Shibata, Y. Zhu, *Corros. Sci.* 36 (1994) 153.
18. T. Shibata, M. Ameer, *Corros. Sci*. 33 (1992) 1633.
19. T. Shibata, *Corros. Sci.* 31 (1990) 413.
20. T. Shibata, Y. Zhu, *Corros. Sci*. 36 (1994) 1735.
21. T. Shibata, Y. Zhu, *Corros. Sci*. 37 (1995) 853.
22. S. Fujimoto, T. Shibata, M. Minamida, S. Udaka, *Corros. Sci*. 36 (1994) 1575.
23. F. Wall, M. Martinez, *J. Electrochem. Soc*., 150 (2003) B146.
24. T. Zhang, C. Chen, Y. Shao, G. Meng, F. Wang, *Electrochim. Acta***,** 53 (2008) 7921.
25. T. Zhang, X. Liu, Y. Shao, G. Meng, F. Wang, *Corros. Sci*. 50 (2008) 3500.
26. G. Meng, L. Zhang, Y. Shao, T. Zhang, F. Wang, *Corros. Sci*. 51 (2009) 1685.
27. G. Meng, L. Wei, Y. Shao, T. Zhang, F. Wang, *J. Electrochem. Soc*., 156 (2009) C240.
28. L. Liu, Y. Li, F. Wang, *Electrochim. Acta***,** 53 (2008) 2453.
29. ASTM Stand G46-94(2005), "Standard Guide for Examination and Evaluation of Pitting Corrosion," ASTM International,West Conshohocken, PA.
30. M. Holzle, U. Retter, D. Kolb, *J. Electroanal. Chem*. 371 (1994) 101.
31. E. Budevski, G. Staikov, W. Lorenz, *Electrochim. Acta* 45 (2000) 2559.
32. M. Jafarian, F. Gobal, I. Danaee, R. Biabani, M. Mahjani, *Electrochim. Acta*, 53 (2008) 4528.
33. F. Varela, E. Codaro, J. Vilche, *J. Appl. Electrochem*. 27 (1997) 1232.
34. R. Armstrong, M. Fleischmann, H. Thirsk, *J. Electroanal. Chem*. 11(1966) 208.
35. M. Moayed, R. Newman, *Corros. Sci*., 48 (2006) 1004.
36. D. Sun, Y. Jiang, Y. Tang, Q. Xiang, C. Zhong, J. Liao, J. Li, *Electrochim. Acta*, 54 (2009) 1558.
37. M. Moayed, R. Newman, *J. Electrochem. Soc*., 153 (2006) B330.
38. P. Pistorius, G. Burstein, *Phil. Trans. R. Soc. Lond. A***,** 341 (1992) 531.
39. X. Liu, Z. Zhan, Q. Liu, *Corros. Sci*., 51 (2009) 1460.
40. A. Valor, F. Caleyo, L. Alfonso, D. Rivas, J. Hallen, *Corros. Sci*. 49 (2007) 559.
41. A. Turnbull, *Br. Corros. J*. 28 (1993) 297.
42. A. Tahara, T. Shinohara, *Corros. Sci*. 47 (2005) 2589.
43. G. Engelhardt, D. Macdonald, *Corros. Sci*. 46 (2004) 2755.
44. A. Trueman, *Corros. Sci*. 47 (2005) 2240.
45. N. Laycock, R. Newman, *Corros. Sci*. 39 (1997) 1771.